Journal of Medical Imaging

MedicalImaging.SPIEDigitalLibrary.org

Characterization and validation of the thorax phantom Lungman for dose assessment in chest radiography optimization studies

Sunay Rodríguez Pérez
Nicholas William Marshall
Lara Struelens
Hilde Bosmans

SPIE.

Sunay Rodríguez Pérez, Nicholas William Marshall, Lara Struelens, Hilde Bosmans, "Characterization and validation of the thorax phantom Lungman for dose assessment in chest radiography optimization studies," *J. Med. Imag.* **5**(1), 013504 (2018), doi: 10.1117/1.JMI.5.1.013504.

Journal of Medical Imaging 5(1), 013504 (Jan–Mar 2018)

Characterization and validation of the thorax phantom Lungman for dose assessment in chest radiography optimization studies

Sunay Rodríguez Pérez,[a,b,*] Nicholas William Marshall,[c] Lara Struelens,[a] and Hilde Bosmans[c]
[a]SCK CEN, Radiation Protection Dosimetry and Calibration, Mol, Belgium
[b]KU Leuven, Medical Physics and Quality Assessment, Leuven, Belgium
[c]UZ Gasthuisberg, Department of Radiology, Leuven, Belgium

Abstract. This work concerns the validation of the Kyoto-Kagaku thorax anthropomorphic phantom Lungman for use in chest radiography optimization. The equivalence in terms of polymethyl methacrylate (PMMA) was established for the lung and mediastinum regions of the phantom. Patient chest examination data acquired under automatic exposure control were collated over a 2-year period for a standard x-ray room. Parameters surveyed included exposure index, air kerma area product, and exposure time, which were compared with Lungman values. Finally, a voxel model was developed by segmenting computed tomography images of the phantom and implemented in PENELOPE/penEasy Monte Carlo code to compare phantom tissue-equivalent materials with materials from ICRP Publication 89 in terms of organ dose. PMMA equivalence varied depending on tube voltage, from 9.5 to 10.0 cm and from 13.5 to 13.7 cm, for the lungs and mediastinum regions, respectively. For the survey, close agreement was found between the phantom and the patients' median values (deviations lay between 8% and 14%). Differences in lung doses, an important organ for optimization in chest radiography, were below 13% when comparing the use of phantom tissue-equivalent materials versus ICRP materials. The study confirms the value of the Lungman for chest optimization studies. [DOI: 10.1117/1.JMI.5.1.013504]

Keywords: anthropomorphic phantom; tissue equivalence; Monte Carlo simulations; optimization; digital radiology; chest radiography; organ dose.

Paper 17307PR received Oct. 13, 2017; accepted for publication Jan. 11, 2018; published online Feb. 6, 2018.

1 Introduction

Phantoms consist of one or more tissue equivalent materials that are combined to simulate the interaction of ionizing radiation inside the body.[1] They can represent different levels of anatomical accuracy, from simple homogeneous blocks to more detailed structures, including internal features mimicking organs. Besides tissue equivalent materials, phantoms can also contain inserts of real human tissue.[2] The development of physical phantoms has continued over time and a wide variety of phantoms are now available.[3] In diagnostic radiology, phantoms are widely used for the optimization of image quality versus dose.[4–7]

Optimization in digital radiology is undertaken to ensure that image quality is sufficient for the radiologist to perform clinical tasks while maintaining a low patient exposure. Optimization studies focus on different parameters of the imaging chain: x-ray source (tube voltage and filtration), antiscatter method (grid or air gap), imaging detector, image processing, and display. To study the influence of these parameters on clinical performance, numerous images comparing different exposure settings are often acquired. While clinical studies offer the gold standard in terms of tasks, realism, and observer performance, there are a number of factors that may preclude their use. For example, a large number of patients, sometimes with a rare pathology, are required to generate statistically meaningful results. This makes optimization a time consuming method in terms of case selection. Case reading may also be problematic for chest radiology procedures, given the broad range of chest tasks that need to be sampled. A further limitation of clinical studies is that results may only apply to patient groups of similar body habitus or pathological condition, as the same patient cannot be imaged repeatedly without clinical justification.

Physical phantoms should therefore be used where relevant. This also applies to chest x-ray imaging, given that new acquisition techniques are developed and deserve detailed studies. Phantoms described in the literature include simple homogeneous types composed of tissue equivalent materials, such as polymethyl methacrylate (PMMA) blocks[8] or more complex phantoms, such as the "Duke" chest phantom.[9] The latter contains copper and aluminum sheets resembling basic anatomical structures, along with circular details used to assess object detectability. This phantom has been previously used to optimize beam quality selection in chest radiography.[10]

In recent years, there has been an evolution in the test objects used in optimization studies, progressing from phantoms with simple homogeneous background to more anthropomorphic phantoms.[11–17] The optimization process can benefit from the use of anthropomorphic phantoms as anthropomorphic phantoms more closely resemble the body anatomy and human tissue composition. This trend is reinforced by developments taking place in the field of 3-D printing technology. With this rapid

*Address all correspondence to: Sunay Rodríguez Pérez, E-mail: srperez@sckcen.be

2329-4302/2018/$25.00

progress, efforts have been made to include structures that simulate real clinical tasks.[18–20] The use of these phantoms as surrogates for real patients for dosimetry studies requires validation of the phantom performance. If the phantom is used for optimizing the detection of certain pathology, then the phantom must not only simulate real human anatomy and pathology but also the interaction of radiation in the tissue. From this, typical minimum dose levels required for diagnostic tasks can be found.

For dose assessment purposes and optimization studies performed as a function of beam quality, the phantom should be made of materials with x-ray absorption properties close to those of human tissue. In this way, results remain accurate as x-ray energy is changed. To optimize system settings, such as automatic exposure control (AEC), the phantom should produce similar exposure parameters as those used for real patients.[21] Parameters that can be used to evaluate this are air kerma area product (KAP) and dose at the detector level assessed by exposure index (EI). This may also require that the phantom is realistic enough that segmentation algorithms function as they would for patient images. Finally, similar image morphology and noise may also be required to optimize processing and display.

The Lungman anthropomorphic chest phantom (Kyoto Kagaku, Tokyo, Japan; Fig. 1) is designed to be used in plain radiography and in CT scanning for protocol optimization. The phantom is supplied with two extra layers of tissue equivalent material (chest plates). These are 27-mm thick, allowing a total additional body thickness of 54 mm to be simulated. The internal structures of the phantom are easily removed so that inserts can be added to represent clinical tasks. Although the Lungman has been used to study chest radiography,[6,17,22] no publications have been found describing how closely the phantom represents patients. Therefore, the aim of this work was to validate the Lungman phantom for dose assessment purposes in chest radiography. The procedure applied was divided into three steps:

1. Establish the PMMA equivalent thickness of the lung and mediastinum regions of the Lungman. This will allow benchmarking against standard (homogeneous) test objects.
2. Compare KAP, exposure time, and EI data for images acquired with the phantom to those of real patients under AEC.
3. Create a voxelized model of Lungman so that a detailed dosimetric comparison can be made between the phantom materials and the materials in ICRP Publication 89.[23]

Fig. 1 Anthropomorphic physical phantom Lungman.

2 Methods

2.1 *Polymethyl Methacrylate Equivalence of the Lungman Phantom*

Three configurations were used when estimating the PMMA equivalence of the Lungman phantom. The first was without tissue layers, then with one layer placed at the back of the phantom, and finally with two layers (one front and one back). Images of the different configurations were acquired for tube voltages ranging between 60 and 120 kVp in steps of 10 kVp. At a given tube voltage, a posterior–anterior (PA) image of the Lungman phantom was acquired under AEC control and the delivered tube current–time product (mAs) recorded. Subsequently, the AEC was deselected and the mAs set to ~1.5 times the mAs delivered by the AEC. This reduced the influence of noise on the measured data and ensured that the detector was not saturated during the acquisitions. These mAs settings (at the specific tube voltage) were used to acquire three Lungman images: standard Lungman, Lungman plus one layer, and Lungman plus two layers. The Carestream "pattern" program was used for all acquisitions. This is a DICOM "for processing" image type provided by the vendor that is suitable for technical evaluations, i.e., with all the necessary detector corrections but without clinical image processing. The phantom was removed and PMMA blocks of dimension 26×30 cm^2 were positioned in its place. Images were then acquired for thicknesses between 10 and 20 cm in steps of 2 cm, using the mAs used for Lungman. This ensures a fixed relationship between x-ray attenuation for the Lungman materials and PMMA, as quantified by the pixel value (PV). The remaining settings were those used in routine clinical practice: a source to image receptor distance of 180 cm and filtration of 2.96 mm of aluminum. The images were exported from the system in DICOM format with a linear look-up table. Subsequently, the mean PV was measured for a 10×10 mm^2 region of interest (RoI) at the center of the PMMA images. The PV was plotted against PMMA thickness for the different tube voltages, and the data points were fitted with an exponential function [Eq. (1)], where T_{PMMA} is PMMA thickness in centimeters:

$$\mathrm{PV} = A \times e^{-B \times T_{\mathrm{PMMA}}}. \tag{1}$$

Using the inverse of the above relationship, the PV data in images of the Lungman acquired at the same exposure parameters (tube voltage and mAs) were converted to equivalent centimeters of PMMA.

2.2 *Comparison of the Lungman Phantom and Real Patients in Terms of Exposure Index, Kerma Area Product, and Exposure Time*

In order to compare phantom exposure data with typical patient data, the phantom was imaged using a Carestream DRX Evolution radiographic system (Carestream, New York) used for chest x-rays in our hospital. The system uses a cesium iodide-based flat panel detector and is generally operated under AEC. Phantom images were acquired using the standard adult chest program. PA projections were taken under standard clinical conditions: tube voltage of 120 kVp, source-to-detector distance of 180 cm, and the antiscatter grid in position. The left and right (lung field) chambers of the AEC device were used. EI, KAP, and exposure time values were recorded and compared to

the values from real patients. The acquisitions were then repeated for the phantom with the additional tissue layers attached.

EI, KAP, and exposure time data of patients were then surveyed for this x-ray room. The survey included 1795 adult patients undergoing chest thorax PA examinations over a 2-year period, from March 2015 to March 2017. The calibration of the integrated KAP meter is verified annually during the medical physics test. The parameter EI is calculated by the system from PV data in a relevant image region, i.e., the segmented anatomy. For this system, EI is calibrated against detector air kerma using the RQA5 beam quality.[24] EI gives an indication of the radiation exposure at the detector entrance used for a given image, and it may depend on the segmentation region used and the body part imaged.[25,26] These data were extracted from DICOM headers using an automated dose management platform (TQM, Qaelum NV, Belgium). Finally, the PMMA thickness that matched the three phantom configurations (Sec. 2.1) was imaged at a patient equivalent position in order to compare the EI and KAP values obtained for the PMMA blocks with those from Lungman and the patients.

2.3 *Creation of a Voxel Model of the Lungman Phantom: Comparison of Organ Absorbed Dose Using Kyoto Kagaku Tissue Equivalent and ICRP Materials*

In the final validation step, a computational model of the Lungman phantom was created. The model was obtained from the segmentation of a 3-D dataset acquired on a Siemens Definition Flash CT scanner using the following parameters: 120 kVp, 450 mA, pixel size of 0.95×0.95 mm^2, and slice thickness of 0.6 mm. CT image segmentation was performed using 3-D slicer [27] and Fiji,[28] both of them open source software packages for visualization and image analysis. Thresholding, region growing, edge detection, and model fitting were used for the delineation of the organs. The segmented organs were then exported as OBJ files, a format that contains the information of the vertexes and the vertex normals of the 3-D objects. For use in Monte Carlo simulations with PENELOPE/penEasy Monte Carlo transport code,[29,30] the OBJ files were then voxelized using software developed by Lombardo.[31] An algorithm was developed in the Python programming language to transform the output from the previous software to a format that can be read by penEasy. This format consisted of a two-column file containing information about material index and density, as well as a header section.

The voxel model of the phantom was used in Monte Carlo simulations to assess the suitability of the Kyoto Kagaku tissue-equivalent materials for dosimetry studies. To this end, two versions of the voxel phantom were created: one using Kyoto Kagaku tissue equivalent materials and another with material composition given in ICRP Publication 89. The absorbed dose in each of the organs was then compared for the two versions. The phantoms were irradiated with a cone beam covering the entire surface of the phantom in PA and anterior–posterior (AP) projections, for tube voltages ranging from 60 to 125 kV. The energy distribution of the source was simulated using the model of Boone and Seibert[32] for a tungsten anode x-ray tube. Spectra for the different energies were provided in penEasy as external text files with 1-keV sampling intervals. The energy deposition tally was used, which scores the energy deposited per simulated history in each organ. The output from the tally was divided by the mass corresponding to each organ to obtain the organ dose for both material types (i.e., Kyoto Kagaku and ICRP). The results were then expressed as a relative deviation from the ICRP material case:

$$R_{\mathrm{dev}} = \frac{D_{\mathrm{KYOTO}} - D_{\mathrm{ICRP}}}{D_{\mathrm{ICRP}}}. \tag{2}$$

Table 1 shows the mass ratios of the Kyoto Kagaku materials used in the Lungman phantom and the corresponding ICRP materials. Chemical composition of the Kyoto-Kagaku tissue equivalent materials in the Lungman was provided by the manufacturer. Due to the complexity of the phantom airways and the spatial resolution of CT images, the smallest structures could not be fully segmented. However, as observed in Fig. 1, the lung region is composed of air and bronchi simulating material, thus the latter is the main contribution to the average lung density in the phantom. To compensate for the lack of true density distribution in the voxel model of the phantom, three different approaches were considered to model the lung material.

The first step was to calculate the average density in the lung region of the CT images. The lung borders were identified and segmented from the surrounding tissue. The average attenuation in the lungs was then calculated by averaging Hounsfield Unit data within this volume. To convert this value to density (g/cm^3), "k-wave," a MATLAB toolbox for simulation of acoustic wave fields, was employed. This toolbox uses the experimental data reported by Schneider et al..[33]

In deciding upon the method to model the lungs, a preliminary study was carried out in which three methods were evaluated. The first approach assumed that the entire lung region was homogenously filled (i.e., segmented bronchi excluded from the model) with a mixture of soft tissue equivalent material and air. The density used for this was calculated previously from the average attenuation in the lungs. The second approach was to include the segmented bronchi and to set lung material to that used for the first approach (mixture of soft tissue and air). However, in this case the mixture density was equal to the average lung density (calculated from the average HU) minus the density contribution given by the bronchi actually segmented in the model. The third approach was to use air in the lungs (as in the physical phantom) and keep the segmented bronchi model as a separate material. For the latter two

Table 1 Ratio between Kyoto Kagaku and ICRP 89 organ masses.

Organs	Kyoto-Kagaku/ICRP organ mass (g)
Thoracic wall	1.117
Ribs	0.701
Diaphragm	1.020
Lungs	0.357
Vertebrae	1.023
Heart	1.028
Bronchi	1.029
Trachea	1.025

approaches, the simulated material was based on the tissue equivalent material reported by the manufacturer.

The reference materials and proportions of mixtures used for the comparison were taken from ICRP Publication 89.[23] Weighted mixtures of trabecular and cortical bones were employed for the bones. Specifically, for the vertebrae, a proportion of 25% cortical and 75% trabecular was used, whereas in the ribs, 94% corresponded to cortical and 6% to trabecular bone.[23] For the thoracic wall, the material used was residual tissue, i.e., a mixture between soft tissue and fat. For the trachea, the material reported in the ICRP was used in the external walls while the inside was filled with air. The diaphragm was filled with skeletal muscle, and the heart with a mixture of 60% blood and 40% heart wall striated muscle. As mentioned before, three methods were considered for simulating the lungs, for the first (i.e., homogenous mixture), the lung material was set as a mixture of air, lung tissue, vessels, bronchi, and blood with average density and composition reported in the ICRP. In the second approach (including segmented bronchi and material mixture in the lungs), the density of the lung mixture was adjusted to include the contribution from the segmented bronchi. In the third approach, air was used to surround the bronchi material. For the last two cases, the bronchi were filled with bronchus material.

The three approaches used for lung modeling were compared in terms of relative deviation of the organ dose between the Kyoto Kagaku and the ICRP materials. When comparing the first and second approach, there was no difference in the relative deviation for the lung dose in both cases. For the second and third case, the relative deviation of the dose in the bronchi varied in less than 2%. Therefore, the second approach was considered the most suitable for modeling the lung since the segmented bronchi were present and the average density of the lung region corresponded to that of the physical phantom.

3 Results

3.1 *Polymethyl Methacrylate Equivalence of the Lungman*

Figure 2 shows the relationship between the average PV for the PMMA images and PMMA thickness, with tube voltages as a parameter. The results of these curve fits were then applied to the Lungman images acquired at the same tube voltage [Eq. (1)]. To establish the PMMA equivalence in different regions of

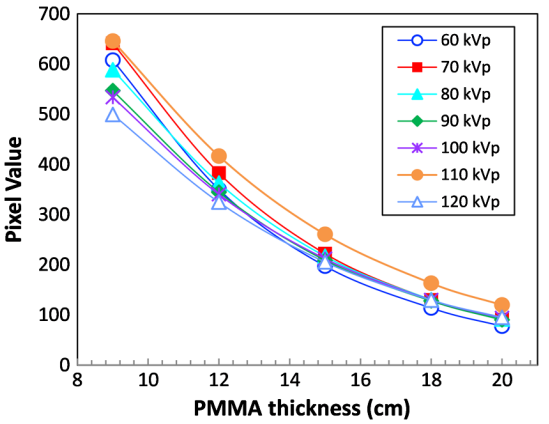

Fig. 2 Relationship between PV and PMMA thickness (fixed mAs for each tube voltage), for the range of tube voltages studied.

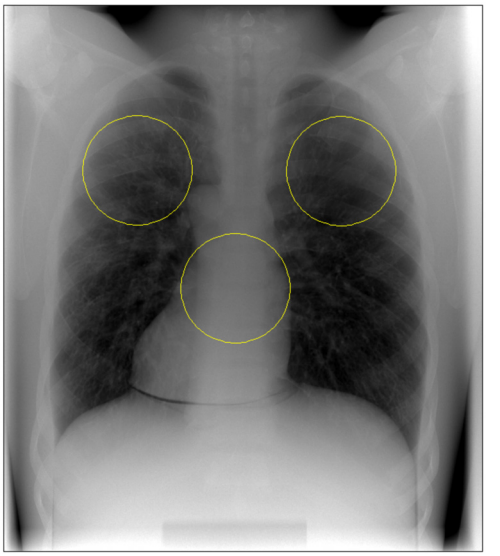

Fig. 3 Image of the Lungman phantom converted to PMMA equivalence. The RoIs drawn correspond to the AEC.

the phantom (i.e., lungs and mediastinum), three RoIs were positioned at locations corresponding to the AEC chamber positions marked on the Bucky (Fig. 3). The mean PV in the PMMA equivalent images from these regions gave the equivalence in centimeters of PMMA of the right and left lungs and the mediastinum at different energies.

Figures 4 and 5 illustrate the PMMA equivalence of the Lungman phantom (including the tissue layers) in the mediastinum and lung regions. The PMMA equivalence curves for the three versions of the phantom have a similar trend. There is a slight increase in PMMA equivalence at higher tube voltages, but overall there is not a strong dependence on energy. For Lungman with no attachments, PMMA equivalence in the mediastinum varied from 13.5 to 13.7 cm, whereas for the lungs (averaged between right and left lungs), the results ranged from 9.5 to 10.0 cm. These results are consistent with data

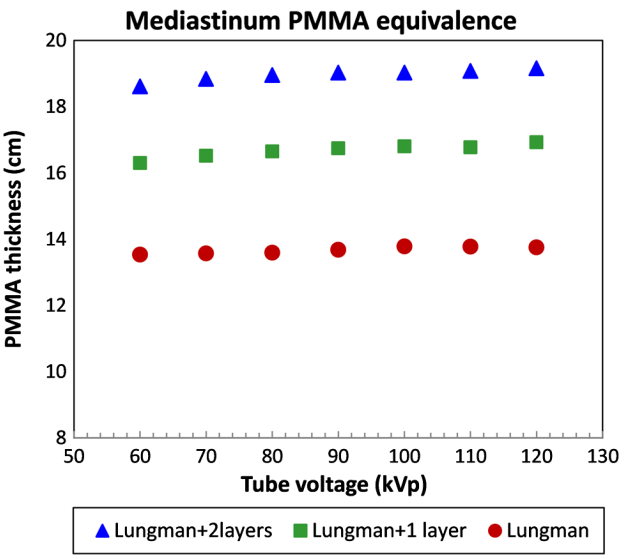

Fig. 4 PMMA equivalence for the mediastinum region in the Lungman phantom and the extra tissue layers as a function of peak tube voltage.

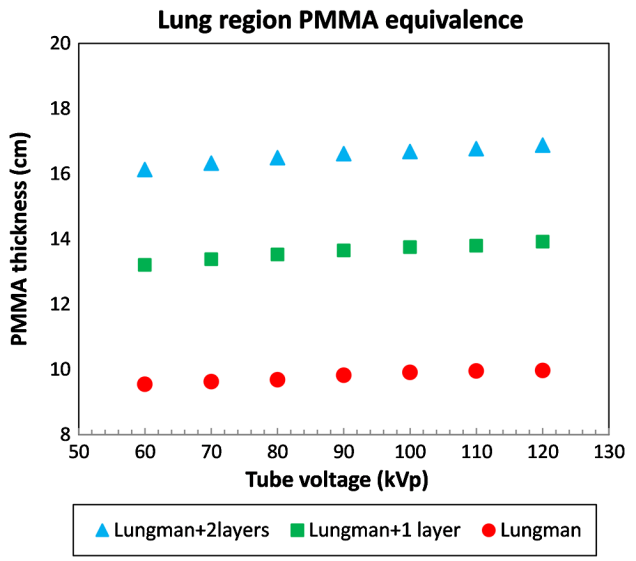

Fig. 5 PMMA equivalence for the lungs' region in the Lungman phantom and the extra tissue layers as a function of peak tube voltage.

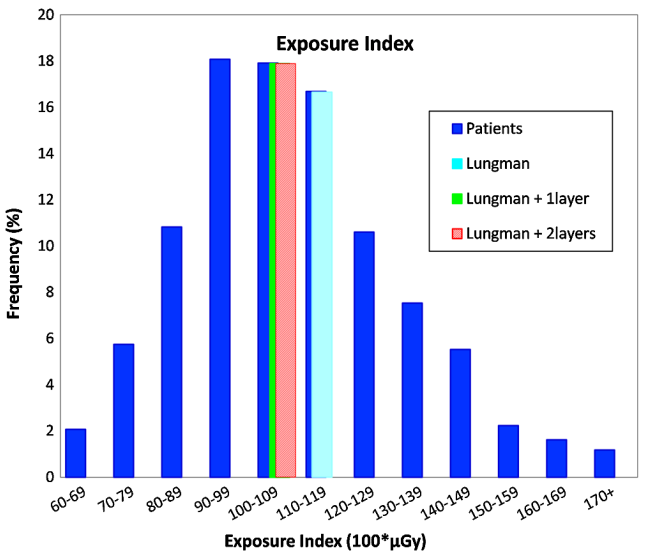

Fig. 7 EI distributions for a range of patients undergoing chest PA examinations with the Carestream system compared with the EI values for the Lungman phantom.

reported by Dobbins et al.,[34] where a PMMA phantom of 9.3-cm thickness was used to simulate the lung tissue thickness for chest radiography. For the phantom data with increased thickness, PMMA equivalence in the mediastinum region ranged from 16.3 to 16.9 cm and from 18.6 to 19.2 cm for one and two additional layers, respectively. In the lung region, these equivalences ranged from 13.2 to 13.9 cm and from 16.1 to 16.9 cm.

3.2 *Comparison of the Lungman Phantom to Patients Using EI, KAP, and Exposure Time*

Patient data distributions of KAP, EI, and exposure time are presented in Figs. 6–8 respectively, along with values obtained for the Lungman phantom with and without the tissue layers. The EI, KAP, and exposure time for the Lungman configurations were compared with the median value of each parameter distribution. Relative differences between the EI median value of the patient distribution and the Lungman phantom ranged from 3% to 8%. The smaller difference was obtained for the Lungman with one tissue layer attached. For the KAP and exposure time distributions, the closest values to the patient median value were found for the Lungman without any extra layers, with 14% deviation in both cases. Once the extra layers were attached, differences of 30% and 100% were obtained for the Lungman with one and two layers, respectively.

These results suggest that the use of Lungman in chest optimization procedures will give EI, KAP, and exposure time values that correspond to those found in typical patient distributions of these parameters. They also indicate that the phantom together with the chest plate is necessary to represent a wider population. As can be seen in the histograms of

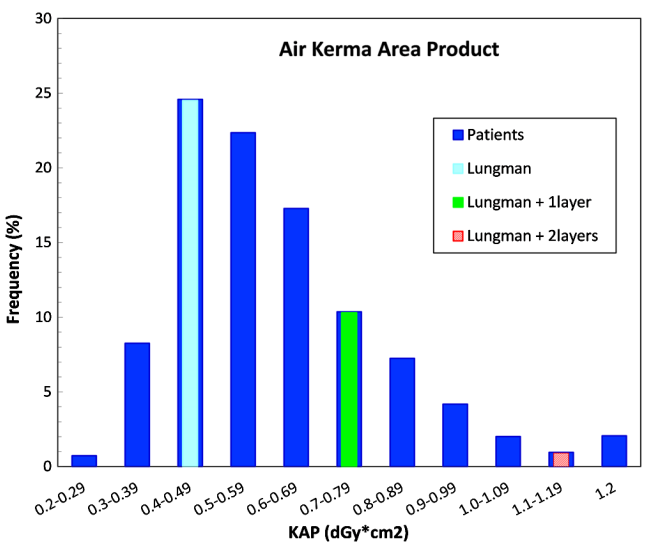

Fig. 6 KAP distributions for a range of patients undergoing chest PA examinations with the Carestream system compared with the KAP values for the Lungman phantom.

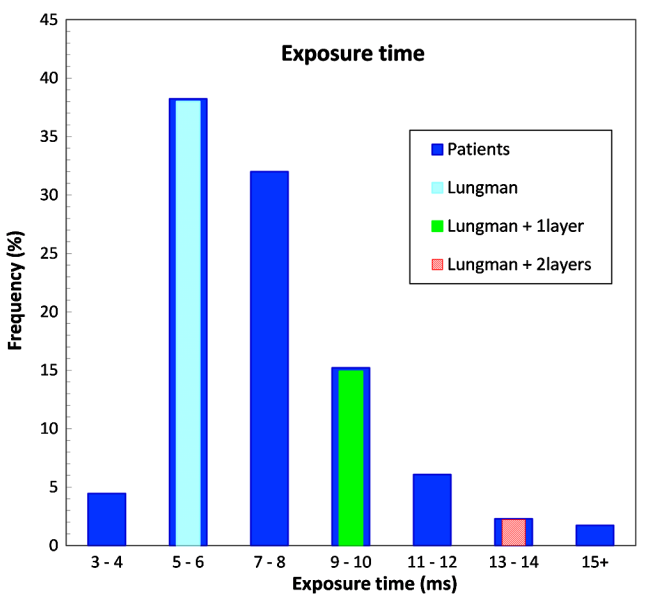

Fig. 8 Exposure time distributions for a range of patients undergoing chest PA examinations with the Carestream system compared with the exposure time values for the Lungman phantom.

Figs. 6–8, the KAP and the exposure time increased when the tissue layers were placed in the phantom (as expected), however, the EI value decreased.

To further study this behavior, the 2-D plot in Fig. 9 was used, in which patient EI data were plotted as a function of KAP for the same examination (blue point cloud). In order to indicate local peak densities, a Gaussian–kernel density estimator was used to apply color mapping to the data. This type of 2-D plot can be employed to study AEC device performance as well as to detect radiographic or technical problems in the system. For a given field size, the AEC device is expected to increase the KAP according to patient thickness in order to keep EI constant. However, as illustrated in the graph, the EI values spread over a range of values rather than being close to some specific target value. A number of factors contribute to this variation in EI value, including variable collimation[35] and segmentation by the EI algorithm. There is also the known dependence of EI with patient thickness:[36] patients with different thickness and anatomy will produce a change in the beam quality, which then influences the EI value.[16]

In Fig. 9, the EI and KAP values corresponding to the Lungman phantom and the PMMA slabs with the lung equivalent thickness of the Lungman are plotted. The PMMA equivalent blocks were imaged at a patient equivalent position using the routine clinical settings for thorax imaging. The three PMMA thicknesses used were 10, 14, and 17 cm, corresponding to the lung region PMMA equivalence of the Lungman phantom including one and two chest plates, respectively. While the KAP values for the PMMA are close to those obtained with the Lungman, values for EI lie some distance from the center of the patient distribution. This is most likely due to segmentation errors in the EI calculation, the accuracy of which may also depend on the body part being imaged.[26] These results suggest that anthropomorphic rather than homogeneous phantoms should be used if EI values are to be investigated.

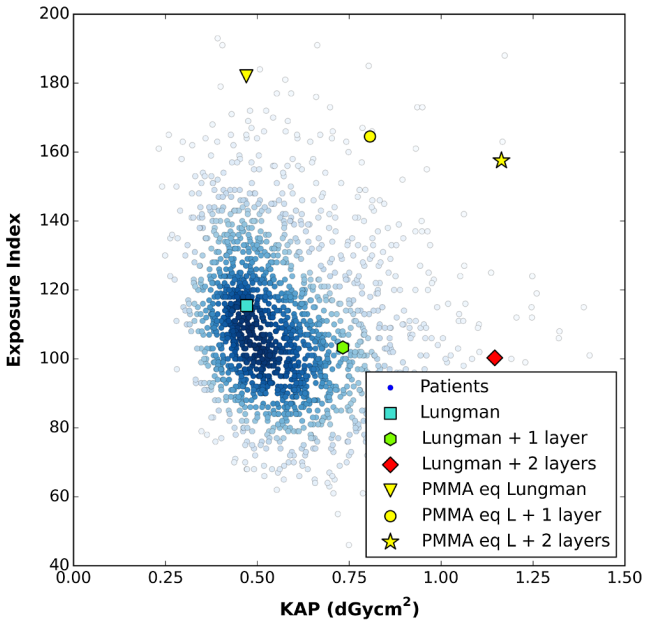

Fig. 9 Patients point cloud of EI as a function of the KAP. EI and KAP values for the Lungman phantom with extra tissue layers and the PMMA equivalence thickness of the lung region of the three phantom configurations are also displayed.

3.3 *Voxelized Model of the Lungman Phantom: Comparison of Organ Dose for ICRP and Kyoto Kagaku Tissue Equivalent Materials*

Eight organs were selected for segmentation from the CT dataset: vertebrae, diaphragm, heart, trachea, bronchus, lungs, thoracic wall, and ribs. The thoracic wall and the ribs were divided into posterior and anterior subsections. Figure 10 illustrates the segmentation result. The voxel model was generated using a resolution of $1.0 \times 1.0 \times 1.0$ mm^3, which represented a compromise between a voxel size sufficient for dosimetry studies and a reasonably low computational load.

Figures 11(a) and 11(b) illustrate the relative deviations between organ absorbed dose using Kyoto Kagaku materials with respect to the ICRP materials as a function of tube voltage, for AP and PA irradiations, respectively.

In the thoracic wall, for the subsection closer to the beam, the organ dose for the Kyoto Kagaku material underestimates the dose for the ICRP material. The opposite is observed for the subsection farther from the beam, which is influenced to a greater extent by the remaining organs. The deviations for this organ do not show a strong x-ray energy dependency, with differences no larger than 17%.

Notable differences were seen in the rib doses, with the largest differences found in the subsection farther from the source (i.e., ribs anterior for PA irradiation and ribs posterior for AP irradiation), where overestimation reached 41%. For this material, the deviations in dose are strongly influenced by the energy of the beam with larger differences at lower energies. On the other hand, for the subsections nearer to the beam, the discrepancies were smaller; underestimations from 2% to 12% were obtained for the dose in the phantom material compared to the dose in the ICRP material.

For the vertebrae in the PA irradiations, dose was overestimated compared to the ICRP materials by 9%. For the AP projection, these differences were greater (from 23% to 32%), with smaller deviations at the higher energy. This can be attributed to the influence of surrounding tissue on the vertebrae dose being larger for AP irradiations.

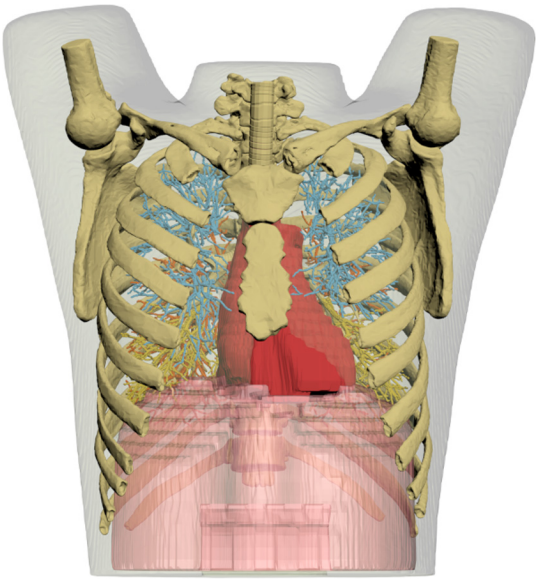

Fig. 10 Segmented organs used for the voxel model of the Lungman phantom.

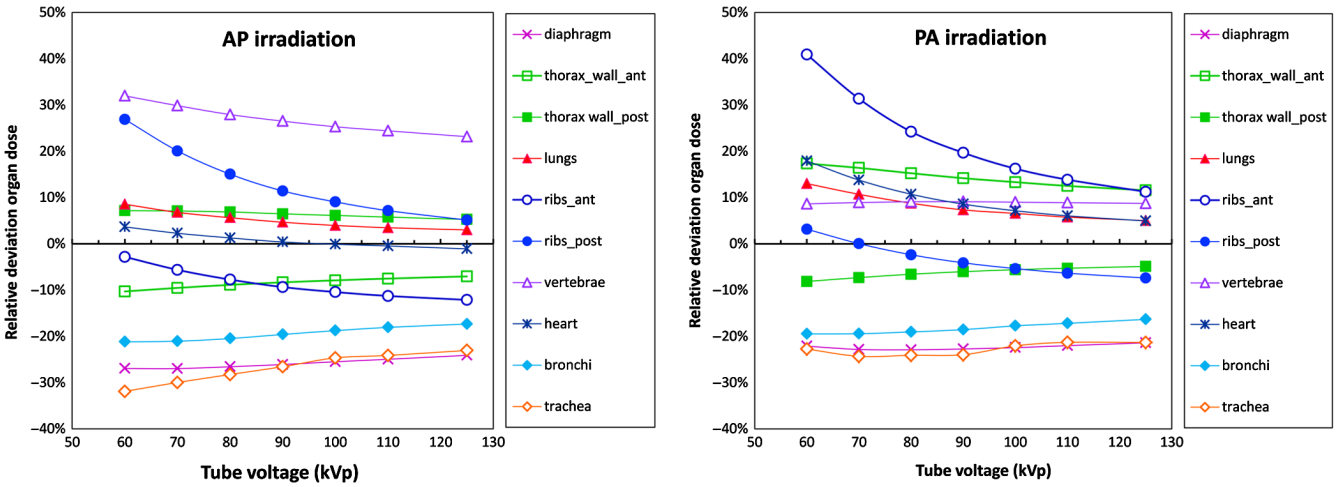

Fig. 11 Relative deviations in the organ absorbed dose using Kyoto Kagaku materials with respect to ICRP materials as function of tube voltage, (a) for AP irradiations and (b) for PA irradiations.

In the diaphragm, the relative deviation has little energy dependence, and the incident beam direction does not have a strong effect. In this case underestimations with respect to ICRP went from 21% to 23% for PA and from 24% to 27% for AP.

For the heart in the AP projection, differences in absorbed dose between the two materials were less than 4%. For PA irradiations differences were larger and showed stronger energy dependence, ranging from 5% to 18%. This can be attributed to the difference in dose deposition in the surrounding organs, especially the ribs and vertebrae being more prominent in PA irradiations.

For the trachea in PA irradiations, dose underestimations ranged from 21% to 24%; in the AP projection, these underestimations increased, ranging from 23% to 32%. It appears that differences for small organs such as this are greatly influenced by the composition of surrounding organs.

For the lungs, doses for the phantom using Kyoto materials gave overestimations compared to the ICRP materials. These deviations went from 3% to 9% for AP data and from 5% to 13% for the PA data. This was expected since the average density of the physical phantom was low compared to the value reported in ICRP. However, these differences are reasonable and do not depend greatly on beam energy. For the case of the bronchi, the dose in the Kyoto Kagaku material underestimated the values obtained using ICRP material. These underestimations were not greatly influenced by the direction or the energy of the beam, with values between 16% and 21%.

4 Discussion

This work has evaluated the suitability of the Lungman thorax phantom for use in dose assessment in chest radiography optimization studies using a three step procedure—a procedure that could be applied on other phantoms. PMMA equivalence of the Lungman was first established. For the lung region of the Lungman with no added layers, the PMMA equivalence varied from 9.5 to 10.0 cm for different energy spectra, which is in line with literature values. PMMA equivalence was also established for thicker versions of the phantom, where one and two chest plates were attached to the phantom. These equivalence estimates should allow comparison of Lungman data to studies that used PMMA as phantom material.

By comparing phantom data with surveyed patient data, it was found that the Lungman and the Lungman with chest plates covered the range of EI, KAP, and exposure time values found in patient data. However, when using the PMMA equivalence corresponding to the lungs, the EI values obtained lay far from the patient distribution. This demonstrates the need for anthropomorphic phantoms containing realistic patient structure when assessing AEC performance with parameters that are sensitive to image content, such as EI.

In the last step, a voxel model of the phantom was developed and used in Monte Carlo simulations to compare the Kyoto Kagaku tissue equivalent materials with those in ICRP Publication 89. The comparison was performed in terms of organ absorbed doses for different energy spectra. Although differences in absorbed dose for the ribs could be as high as 41%, this occurred in the region farther from the x-ray source, where surrounding materials had a stronger influence on doses. For the lungs, a crucial organ when using the phantom for optimization studies, these deviations were less than 13%. The differences found in absorbed dose can be attributed to the influence of surrounding organs; this is the case for small organs like the trachea. Additionally, differences in material composition clearly create discrepancies and reflect the difficulty in manufacturing tissue equivalent materials. Notwithstanding these problems, the voxel model of the phantom could be used in dosimetric studies. On the other hand, when physical survey measurements of x-ray installations are required, the physical version of the Lungman phantom is the obvious alternative to simulations.

The main limitation of the study lies in the accuracy of the voxel phantom representation of the true phantom. In the creation of the voxel phantom via segmentation of tomographic images, the CT voxel size sets a clear limit on resolution of the acquired dataset and the level of detail possible in the voxel phantoms. The knock-on effect was a difficulty in the accurate segmentation of all the airway structures within the phantom. Ultimately this led to errors in the density calculation and therefore in the final dose calculation.

5 Conclusion

The findings of this study suggest that the Lungman phantom can be considered an appropriate anthropomorphic phantom for

dose and AEC performance evaluation of x-ray systems in the diagnostic imaging energy range.

Disclosures

The authors do not have conflict of interest or financial interest to declare.

References

1. X. G. Xu, "Computational phantoms for organ dose calculations in radiation protection and imaging," in *The Phantoms of Medical and Health Physics: Devices for Research and Development*, L. A. DeWerd and M. Kissick, Eds., pp. 225–262, Springer, New York (2014).
2. D. R. White et al., "Report 48. Phantoms and computational models in therapy, diagnosis and protection," *J. Int. Comm. Radiat. Units Meas.* **os25**(1) (1992).
3. D. Hintenlang, W. Moloney, and J. Winslow, "Physical phantoms for experimental radiation dosimetry," in *Handbook of Anatomical Models for Radiation Dosimetry*, X. G. Xu and K. F. Eckerman, Eds., pp. 389–409, Taylor and Francis, New York, Tennessee (2009).
4. J. T. Dobbins, III et al., "Chest radiography: optimization of x-ray spectrum for cesium iodide-amorphous silicon flat-panel detector," *Radiology* **226**(1), 221–230 (2002).
5. T. M. Bernhardt et al., "Low-voltage digital selenium radiography: detection of simulated interstitial lung disease, nodules, and catheters —a phantom study," *Radiology* **232**(3), 693–700 (2004).
6. M. Båth et al., "Method of simulating dose reduction for digital radiographic systems," *Radiat. Prot. Dosim.* **114**(1–3), 253–259 (2005).
7. C. S. Moore et al., "Correlation of the clinical and physical image quality in chest radiography for average adults with a computed radiography imaging system," *Br. J. Radiol.* **86**(1027), 20130077 (2013).
8. P. Toroi, K. C. Young, and G. Marchal, "Experimental investigation on the choice of the tungsten/rhodium anode/filter combination for an amorphous selenium-based digital mammography system," *Eur. Radiol.* **17**, 2368–2375 (2007).
9. H. G. Chotas et al., "Digital chest radiography with photostimuable storage phosphors: signal-to-noise ratio as a function of kilovoltage with matched exposure risk," *Radiology* **186**, 395–398 (1993).
10. P. Doyle, C. J. Martin, and D. Gentle, "Dose-image quality optimisation in digital chest radiography," *Radiat. Prot. Dosim.* **114**(1–3), 269–272 (2005).
11. J. Vassileva, "A phantom for dose-image quality optimization in chest radiography," *Br. J. Radiol.* **75**(898), 837–842 (2002).
12. D. R. Pina et al., "Optimization of standard patient radiographic images for chest, skull and pelvis exams in conventional x-ray equipment," *Phys. Med. Biol.* **49**(14), N215 (2004).
13. U. Rapp-Bernhardt et al., "Experimental evaluation of a portable indirect flat-panel detector for the pediatric chest: comparison with storage phosphor radiography at different exposures by using a chest phantom," *Radiology* **237**(2), 485–491 (2005).
14. G. Ullman et al., "Towards optimization in digital chest radiography using Monte Carlo modelling," *Phys. Med. Biol.* **51**(11), 2729–2743 (2006).
15. G. Ullman et al., "A Monte Carlo-based model for simulation of digital chest tomosynthesis," *Radiat. Prot. Dosim.* **139**(1–3), 159–163 (2010).
16. M. Sandborg et al., "Comparison of clinical and physical measures of image quality in chest and pelvis computed radiography at different tube voltages," *Med. Phys.* **33**(11), 4169–4175 (2006).
17. W. K. Ma et al., "Anthropomorphic chest phantom imaging—the potential for dose creep in computed radiography," *Radiography* **19**(3), 207–211 (2013).
18. D. B. Williams et al., "Optimal kVp selection for dual-energy imaging of the chest: evaluation by task-specific observer preference tests," *Med. Phys.* **34**(10), 3916–3925 (2007).
19. J. Solomon and E. Samei, "Quantum noise properties of CT images with anatomical textured backgrounds across reconstruction algorithms: FBP and SAFIRE," *Med. Phys.* **41**(9), 091908 (2015).
20. L. Cockmartin et al., "Design and application of a structured phantom for detection performance comparison between breast tomosynthesis and digital mammography," *Phys. Med. Biol.* **62**(3), 758–780 (2017).
21. B. J. Conway et al., "Beam quality independent attenuation phantom for estimating patient exposure from x-ray automatic exposure controlled chest examinations," *Med. Phys.* **11**(6), 827–832 (1984).
22. B. Renger et al., "Evaluation of dose reduction potentials of a novel scatter correction software for bedside chest x-ray imaging," *Radiat. Prot. Dosim.* **169**(1–4), 60–67 (2016).
23. ICRP, "Basic anatomical and physiological data for use in radiological protection: reference values. ICRP publication 89," *Ann. ICRP* **32**(3–4) (2002).
24. IEC, "Medical diagnostic x-ray equipment—radiation conditions for use in the determination of characteristics," International Electrotechnical Commission (IEC), IEC 61267, Geneva (2005).
25. IEC, "Medical electrical equipment—exposure index of digital x-ray imaging systems—part 1: definitions and requirements for general radiography," International Electrotechnical Commission (IEC), IEC 62494-1, Geneva (2008).
26. S. J. Shepard et al., "An exposure indicator for digital radiography: AAPM Task Group 116 (executive summary)," *Med. Phys.* **36**, 2898–2914 (2009).
27. A. Fedorov et al., "3D slicer as an image computing platform for the quantitative imaging network," *Magn. Reson. Imaging* **30**(9), 1323–1341 (2012).
28. J. Schindelin et al., "Fiji: an open-source platform for biological-image analysis," *Nat. Methods* **9**(7), 676–682 (2012).
29. F. Salvat et al., "PENELOPE—a code system for Monte Carlo simulation of electron and photon transport," in *Workshop Proc.*, p. 384 (2006).
30. J. Sempau, A. Badal, and L. Brualla, "A PENELOPE-based system for the automated Monte Carlo simulation of clinacs and voxelized geometries—application to far-from-axis fields," *Med. Phys.* **38**(2011), 5887–5895 (2011).
31. P. A. Lombardo, "Development of flexible computational phantoms for dosimetric applications," PhD Dissertation, Katholieke Universiteit Leuven (2018).
32. J. M. Boone and J. A. Seibert, "An accurate method for computer-generating tungsten anode x-ray spectra from 30 to 140 kV," *Med. Phys.* **24**(11), 1661–1670 (1997).
33. U. Schneider, E. Pedroni, and A. Lomax, "The calibration of CT Hounsfield units for radiotherapy treatment planning," *Phys. Med. Biol.* **41**(1), 111–124 (1996).
34. J. T. Dobbins et al., "Threshold perception performance with computed and screen-film radiography: implications for chest radiography," *Radiology* **183**, 179–187 (1992).
35. U. Mothiram et al., "Digital radiography exposure indices: a review," *J. Med. Radiat. Sci.* **61**, 112–118 (2014).
36. T. Takaki et al., "Evaluation of the effects of subject thickness on the exposure index in digital radiography," *Radiol. Phys. Technol.* **9**(1), 116–120 (2016).

Sunay Rodríguez Pérez is a PhD student at Katholieke Universiteit Leuven and the Belgian Nuclear Research Centre (SCK-CEN), Belgium. She received her BSc and MSc degrees in nuclear physics, from the Higher Institute of Technologies and Applied Sciences (InSTEC), Havana, Cuba, in 2012 and 2014 respectively. Her PhD focuses on the creation of a simulation framework for task based optimization studies in chest radiography.

Nicholas William Marshall is a medical physicist at the University Hospital of KU Leuven since 2009, helping with research into medical x-ray imaging, with emphasis on detector and system evaluation. Previously, he held positions at the Regional Medical Physics Department at Newcastle upon Tyne, the Clinical Physics Group at Barts and the Royal London Hospital Trust. He received his PhD from the University of Newcastle upon Tyne, and his BSc from Imperial College in London.

Lara Struelens has a physics background with a specialization in medical physics. In 2005, she obtained a PhD in applied physics on the topic "Optimization of patient doses, linked to image quality, for interventional radiology". She is a researcher at the Belgian

Nuclear Research Centre (SCK•CEN) in the expert group "Radiation Protection Dosimetry and Calibration" since 2000. In 2014, she became head of the unit "Research in Dosimetric Application" within the expert group.

Hilde Bosmans is professor and medical physics expert in the University Hospital of KU Leuven. With her team she ensures medical physics services in the radiology department of the University Hospital, in several other hospitals and in the Belgian breast cancer screening. Research focuses on patient dosimetry, automated quality measures and new techniques in x-ray and MR imaging. The aim of all projects is to understand, then optimize quality and patient dose in medical imaging.